High-resolution all-sky land surface temperature and net radiation over Europe

Dominik Rains[1], Isabel Trigo[2], Emanuel Dutra[2], Sofia Ermida[2], Darren Ghent[3], Petra Hulsman[1], Jose Gómez-Dans[4], and Diego G. Miralles[1]

[1]Hydro-Climate Extremes Lab (H-CEL), Ghent University, Ghent, Belgium
[2]Instituto Português do Mar e da Atmosfera, Lisboa, Portugal
[3]University of Leicester, Space Research Centre, Leicester, United Kingdom
[4]University College London, United Kingdom

Correspondence: Dominik Rains (dominik.rains@ugent.be)

Abstract. Land Surface Temperature (LST) and Surface Net Radiation (SNR) are vital inputs for many land surface and hydrological models. However, current remote sensing datasets of these variables come mostly at coarse resolutions. Although high-resolution LST and SNR retrievals are available, they have large gaps due to cloud-cover that hinder their use as input in models. Here, we present a downscaled and continuous daily LST and SNR product across Europe for 2018–2019. The LST product is based on all-sky LST retrievals from the Spinning Enhanced Visible and InfraRed Imager (SEVIRI) onboard the geostationary Meteosat Second Generation (MSG) satellite, and clear-sky LST retrievals from the Sea and Land Surface Temperature Radiometer (SLSTR) onboard the polar-orbiting Sentinel 3 satellites. The product combines the medium spatial (approx. 5–7 km) but high temporal (30 minute) resolution, gap-free data from MSG, with the low temporal (2–3 days) but high spatial (1 km) resolution of the Sentinel 3 LST retrievals. The resulting 1 km and daily LST dataset is based on an hourly merging of both datasets through bias-correction and Kalman Filter assimilation. Longwave outgoing radiation is computed from the merged LST product in combination with MSG-based emissivity data. Shortwave outgoing radiation is computed from the incoming shortwave radiation from MSG and downscaled albedos using 1 km PROBA-V data. MSG incoming shortwave and longwave radiation and the outgoing radiation components at 1 km spatial resolution are used together to compute the final daily SNR dataset in a consistent manner. Validation results indicate an improvement of the root mean squared error by ca. 8% with a substantial increase in spatial detail compared to the original MSG product. The resulting pan-European LST and SNR dataset can be used for hydrological modelling and as input to models dedicated to estimating evaporation and surface turbulent heat fluxes and will be regularly updated in the future.

1   Introduction

20   The Earth radiation budget describes how the Earth gains energy from the sun (shortwave radiation), and loses energy back to space through its reflection and the emission of thermal (longwave) radiation (Dewitte and Clerbaux, 2017; Kato et al., 2018). Due to the geometry of the Earth orbit around the Sun, the yearly average net radiation at the bottom-of-atmosphere, namely the Surface Net Radiation (SNR), is positive at the equator and decreases towards the poles. This geographical energy imbalance is the main driver of the global atmospheric and oceanic circulation, which transports this energy surplus from the equator

25   towards the poles (Dewitte and Clerbaux, 2017; Kato et al., 2018). SNR is thus a key driver in explaining the distribution of different climate regions and ecosystems on Earth (Köppen and Geiger, 1936), and it dominates the dynamics of biospheric and hydrological processes (Chapin et al., 2002). For this reason, SNR is used as forcing variable in many land surface models, hydrological models and satellite-based retrieval algorithms to estimate (e.g.) evaporation, runoff, soil moisture or surface heat fluxes.

30   The top-of-atmosphere radiation components can be derived directly from satellites. However, dynamic atmospheric (e.g., cloud and aerosol optical depth) and land (e.g. emissivity, LST, albedo or biomass) properties make it more challenging to obtain radiation estimates at the bottom-of-atmosphere, which are much more relevant to the above-mentioned biospheric and hydrological processes. As it is transmitted through the atmosphere, incoming shortwave radiation is scattered and absorbed by aerosols, gases and clouds, changing the temperature of the atmosphere and its emission of longwave radiation in all directions.

35   The radiation reaching the surface is partly reflected depending on land cover and surface conditions and again interacts with the atmosphere/clouds once reflected. According to Stephens et al. (2012), on average 12% of the radiation reaching the surface is reflected back into the atmosphere; this is known as the planetary albedo. Then, part of the incoming radiation absorbed at the land surface is emitted towards the atmosphere as longwave radiation, as described by the Stefan–Boltzmann law. The modelling of these atmospheric and surface processes is required to obtain SNR – i.e. the balance between shortwave and

40   longwave incoming and outgoing radiation at the surface – and it makes satellite-based SNR retrievals indirect and uncertain (Kato et al., 2018).

   Over the past decades, numerous satellites/instruments have been launched to enable the monitoring of the radiation budget. Examples of programmes exploiting these observations to produce long-term global reliable estimates of the individual SNR components (i.e. shortwave and longwave, and both incoming and outgoing) are the International Satellite Cloud Climatology

45   Project (ISCCP, Young et al. (2018)) and the Clouds and the Earth's Radiant Energy System (CERES) project (Wielicki et al., 1996). A comparison between the CERES product and radiation estimates from global reanalyses is given by Jia et al. (2018). Nonetheless, both satellite-based and reanalysis SNR products are mostly provided at a coarse (ca. 0.25°) spatial resolution. This makes them suitable for global analysis or as input in global land surface models, but insufficient for most regional-scale studies. Nonetheless, a few studies have already attempted to produce SNR data at higher spatial resolutions. For instance,

50   Verma et al. (2016) proposed a method to yield a global 5 km SNR product at 8-day resolution by combining high-resolution variables derived from the Moderate Resolution Imaging Spectroradiometer (MODIS) Aqua satellite (including clear-sky land surface temperature (LST), emissivity, aerosol optical depth and albedo) and a radiative transfer model. As an alternative, to

achieve a similar spatial but higher temporal resolutions (e.g. sub-daily or daily), observations from geostationary satellites can be used. The Satellite Applications Facility (LSAF) programme uses observations from the SEVIRI instrument onboard
55 the Meteosat Second Generation (MSG) satellite to produce a dataset at a spatial resolution of ca. 5–7 km (Trigo et al., 2011). Nonetheless, these resolutions appear still insufficient for regional water and agricultural management assessments in heterogeneous landscapes.

In this study, we present a 1 km LST and SNR dataset for Europe using MSG and polar orbiting observations. It is based on combining hourly incoming shortwave/longwave radiation retrievals from the above-mentioned LSAF programme at moderate
60 (5–7 km) spatial resolution with hourly outgoing shortwave/longwave estimates based on those geostationary observations as well as higher resolution (1 km) observations from PROBA-V and Sentinel 3 (Donlon et al., 2012). The methodology can be extended to other regions where geostationary-based radiation retrievals are available, and adapted to work with other high-resolution polar data. The merged hourly SNR and LST data is for robustness resampled to daily time steps to serve as input to models or for other analysis. The data and method are presented in detail in sections 2 and 3. All input and derived
65 radiation components are validated against *in situ* measurements sites located across the study domain (section 4). Finally, a discussion and concluding remarks is given in section 5. The daily SNR and LST datasets are available for scientific use under https://doi.org/10.5281/zenodo.7008066 / https://doi.org/10.5281/zenodo.7026612 as netcdf files (RNETdaily_lon_lat.nc and LSTdaily_lon_lat.nc), see Rains (2022a) and Rains (2022b).

2 Data

70 Table 1 provides a general overview of the satellite data products used in this study. Shortwave and longwave incoming radiation components, SW_{in} and LW_{in}, as well as emissivity ε, albedo α and LST are provided by LSAF (lsa-saf.eumetsat.int) and are based on observations from the Spinning Enhanced Visible and InfraRed Imager (SEVIRI) instrument onboard the Meteosat Second Generation (MSG) geostationary satellite. These MSG products are provided with a 30-minute sampling, but to reduce data volumes we base our methodology on hourly data. The spatial resolution across the European domain is
75 approximately 5–7 km depending on latitude. In addition, 1 km LST retrievals from the Sea and Land Surface Temperature Radiometer (SLSTR) instrument onboard Sentinel 3 as well as 1 km albedo retrievals from PROBA-V are used to compute the high-resolution LST dataset and outgoing radiation components. For the purpose of validation, we use radiation measurements from sites distributed across Europe belonging to different international networks. A more detailed description of the satellite retrievals and *in situ* data used in the study is provided in the following subsections.

80

Variable	Satellite	Orbit	Temporal	Spatial	Coverage
SW_{in}	MSG	geostationary	hourly	5–7 km	all-sky, clear-sky+model
LW_{in}	MSG	geostationary	hourly	5–7 km	all-sky, clear-sky+model
LST	MSG	geostationary	hourly	5-7 km	all-sky, clear-sky+model
LST	Sentinel 3A	polar	2–3 days	1 km	clear-sky
ε	MSG	geostationary	daily	5–7 km	clear-sky composite
α	MSG	geostationary	daily	5–7 km	clear-sky composite
α	PROBA-V	polar	10-daily	1 km	clear-sky composite

Table 1. Overview of satellite based products used in the study with their respective temporal and spatial resolution as well as their coverage, i.e. clear-sky vs. all-sky.

2.1 Incoming shortwave/longwave radiation

We use hourly data from the LSAF programme, part of the distributed Applications Ground Segment SAF network serving as the European organisation for the Exploitation of Meteorological Satellites (EUMETSAT). The data are based on observations provided by SEVIRI onboard MSG, acquired at 12 spectral channels with 3 km resolution at nadir (1 km for the high-resolution visible channel) (Trigo et al., 2011). A detailed description of the LSAF methodology on deriving SW_{in} and its validation is given by Carrer et al. (2019a) and Carrer et al. (2019b). Details on the estimation and evaluation of LW_{in} are given by Trigo et al. (2010) and Carrer et al. (2012).

2.2 LST

The LSAF all-sky LST product based on the SEVIRI instrument onboard the geostationary Meteosat Second Generation (MSG, Martins et al. (2019)) is a combination of the clear-sky MSG level 2 product, MSLT (LSA-001), based on a Generalised Split-Window (GSW) algorithm (Trigo et al., 2008a), and output from an energy balance algorithm which is also used for the estimation of MSG 30-minute evaporation (MET-v2, LSA-311) dataset (Ghilain, 2016). The energy balance algorithm incorporates other LSAF SEVIRI-based products such as shortwave and longwave radiation fluxes, land surface albedo or vegetation, soil moisture based on the assimilation of scatterometer observations provided by the Hydrology SAF (H-SAF), and near surface meteorological information obtained from the European Centre for Medium-Range Weather Forecasts (ECMWF) operational forecasts (Ghilain et al., 2020). Within the model, each pixel is composed of different tiles representing a particular surface type based on the ECOCLIMAP-II database (Faroux et al., 2013). Pixel values are computed from the weighted average of the four most dominant tiles. The advantage of using geostationary satellites is the high temporal resolution, allowing for the characterisation of the LST diurnal cycle. An assessment of the accuracy of the LST is given by Martins et al. (2019). The

100   product comes with gridded uncertainty estimates, which are used in the LST merging procedure.

Higher-resolution, clear-sky LST estimates are obtained from Sentinel 3. The Sentinel 3 mission consists of two polar-
orbiting satellites (Sentinel 3A/B) launched on February 16, 2016, and April 25, 2018 (Ghent et al., 2017; Zheng et al.,
2019; Nie et al., 2021), both carrying the Sea and Land Surface Temperature Radiometer (SLSTR) instrument. They have

105   a revisit time of 2–3 days. The instrument has nine channels, three of them covering the visible and near-infrared (VNIR)
part of the spectrum, three the shortwave infrared (SWIR), and the remaining three the middle-infrared (MIR and TIR, Nie
et al. (2021)). For this study, we use the Climate Change Initiative (CCI) LST product provided at a spatial resolution of 0.01
degrees (https://climate.esa.int/en/odp//project/land-surface-temperature). Included in the product is the exact overpass time
and as for the LSAF LST from MSG the total estimated uncertainty for each retrieval, necessary for the merging of the polar

110   and geostationary LST data. For the initial daily SNR product (2018–2019) we only use retrievals from Sentinel 3A and not
Sentinel 3A/B. (see section 3.3).

2.3 Surface emissivity

Land surface ε is required, in conjunction with LST, to calculate LW_{out}. Approaches to retrieve ε can be broadly separated into
methods where LST and ε are jointly retrieved or where ε is retrieved in isolation. The latter was initially used within the LSAF

115   programme, and relied on spectral data for the various land covers based on spectral libraries, and dynamic land cover fractions
(Peres and DaCamara, 2005). To overcome difficulties linked to performing the retrieval of LST and ε separately under certain
conditions, e.g. in semiarid regions, LST and ε are now simultaneously retrieved by the LSAF programme including for the
products we use in this study (Trigo et al., 2008b).

2.4 Albedo

120   The LSAF α product based on the MSG SEVIRI instrument is produced following three steps: (1) an atmospheric correction
of top-of-atmosphere measurements to obtain reflectances, (2) a daily inversion of a semi-empirical model of the bidirectional
reflectance distribution function, and then the consideration of all inversions within a temporal window to reduce the impact
of outliers and reduce data gaps, and (3) the angular integration for each channel and the spectral integration (Geiger et al.,
2008; Carrer et al., 2018). The product thus describes the hemispherical broadband α. As a second hemispherical broadband

125   α product, we use 1 km retrievals based on ProbaV and distributed through the Copernicus Global Land Service (CGLS). The
retrieval follows the same methodology as for the LSAF α product using observations from the MSG satellite.

2.5 *In situ* measurements

For the validation of the merged hourly/daily SNR dataset we use radiation measurements taken at 46 sites distributed across
Europe for the 2-year study period (2018–2019). Measurements are obtained from the Baseline Surface Radiation Network

130   (BSRN) (Driemel et al., 2018), the European Fluxes Database Cluster (http://www.europe-fluxdata.eu, EFDC), the Integrated

Carbon Observation System (ICOS) (Heiskanen et al., 2021), the FLUXNET-CH4 network (Delwiche et al., 2021), and SAPFLUX (Poyatos et al., 2021).

3 Methodology

3.1 SNR calculation

135 SNR is computed using the radiation balance equation (1).

$$SNR = (SW_{in} + LW_{in}) - (SW_{out} + LW_{out}) \tag{1}$$

where SW_{in} is hourly incoming shortwave radiation (W m^{-2}) and LW_{in} is hourly incoming longwave radiation (W m^{-2}), both from LSAF (see section 2). SW_{out} and LW_{out} are hourly outgoing shortwave and outgoing longwave radiation (W m^{-2}), respectively, calculated as:

140
$$SW_{out} = SW_{in} * \alpha \tag{2}$$

$$LW_{out} = \varepsilon * \sigma * LST^4 + (1 - \varepsilon) * LW_{in} \tag{3}$$

with σ being the Stefan–Boltzmann constant (i.e. 5.67 x 10^{-8} W m^{-2} K^{-4}). Both SW_{out} and LW_{out} are to a large degree controlled by land surface properties and processes, i.e. SW_{out} by α (equation 2), and LW_{out} by ε and LST (equation 3). LST,

145 in particular, dictates the magnitude and variability of LW_{out} over different spatial and temporal scales. Note that the term $(1 - \varepsilon) * LW_{in}$ accounts for longwave reflection (Maes and Steppe, 2012).

The focus here is on the improvement of the spatial resolution of the LSAF SW_{out} and LW_{out} by using gap-free all-sky 1 km α and LST in equations 2 and 3, respectively. The details of these datasets are given in section 3.2 and 3.3. The rationale

150 is based on the assumption that SW_{out} and LW_{out}, especially on the daily scale which we aggregate to, are spatially more heterogeneous than the incoming components. Therefore, by using higher-resolution α and LST, the final SNR dataset can better capture the variability induced by landscape features and conditions.

3.2 Bias correction of albedo

To obtain a spatially and temporally gap-free α dataset at 1 km resolution, we bias-correct the daily α from LSAF towards

155 the retrievals from ProbaV using the mean of the temporally overlapping retrievals for 2018–2019. Remaining gaps are filled through linearly interpolating/extrapolating based on the nearest data points. Prior to the bias correction, the α products are regridded using nearest-neighbour interpolation to a common 0.01° grid. Since both sets of α are based on the same methodology, we assume that the bias can be largely attributed to the difference in spatial resolution, the MSG product integrating multiple observations per day, and possibly to the differences in the channels (ProbaV and SEVIRI) response functions.

3.3 Merging of LST

The merging of the hourly LSAF LST (5–7 km) and Sentinel 3 LST (1 km) relies on the assumption that the diurnal cycle of LSAF is reliable in relative terms, whereas the Sentinel 3 LST can be trusted in absolute terms. This approach allows us to benefit from the high temporal resolution of the geostationary data and the high spatial resolution of the Sentinel 3 observations. After regridding the LSAF observations using nearest-neighbour interpolation to the $0.01°$ grid of Sentinel 3 observations, we follow a stepwise approach:

1. Temporal normalisation of Sentinel 3 daytime/nighttime observations to the full hour.

   The Sentinel 3 LST is available every ~2–3 days both during daytime (~10 am local time) and nighttime (~10 pm local time), conditioned on the presence of clear-skies. However, because of differing overpass times from day to day we first normalise Sentinel 3 daytime/nighttime observations individually to the full hour, using information from the diurnal cycle described by the hourly LSAF observations. For that, at each given grid cell, we compute the mean daytime and nighttime overpass time (in UTC) of the Sentinel 3 observations separately and round these to the full hour. Then, when a Sentinel 3 daytime or nighttime observation is acquired, e.g. prior to that mean daytime or nighttime overpass hour t, the observation is corrected through linear interpolation using the LSAF LST retrievals at t and the previous hour $t-1$ on that day:

   $$Sentinel3LST_{nor} = Sentinel3LST + \Delta t * (LSAFLST_t - LSAFLST_{t-1})$$

   with Δt being the difference between the full hour mean nighttime/daytime overpass time t and the exact overpass time of the Sentinel 3 observation. We do not perform the linear interpolation if $LSAFLST_{t-1}$ and/or $LSAFLST_t$ are not clear-sky observations, and in that case, we disregard the Sentinel 3 observation. This is based on the assumption that the diurnal cycle will be less accurate when mixing clear-sky/all-sky estimates or fully relying on modelled all-sky estimates. Sentinel 3 observations with a Δt of more than 45' (i.e. Δt>0.75) are equally excluded to reduce errors from the linear interpolation.

2. Bias-correction of daytime/nightime LSAF observations towards the normalised, high spatial resolution, Sentinel 3 day-time/nighttime observations.

   The previously individually normalised Sentinel 3 observations $Sentinel3LST_{nor}$ are used as the basis to bias-correct the geostationary observations at the same mean full hour overpass time t (daytime and nighttime separately) per grid cell using the means based on overlapping $Sentinel3LST_{nor}$ and $LSAFLST_t$ observations for the entire 2018–2019 record.

3. Bias-correction of the full hourly geostationary $LSAFLST$ time series per grid cell by assuming that the bias corrected for in the previous steps applies to the subsequent hourly observations too.

   We use the bias correction that was applied to the geostationary daytime observations at the mean Sentinel 3 overpass time to all hours of the same day after the mean Sentinel 3 overpass time and until the mean Sentinel 3 nighttime overpass

time. Then apply the nighttime correction until next daytime overpass time etc.

195   4. Assimilation of the normalised Sentinel 3 observations $Sentinel3LST_{nor}$ from Step 1 into the bias-corrected hourly geostationary LSAF LST time series from Step 3.

At a given pixel and point in time when both $LSAFLST$ and $Sentinel3LST_{nor}$ are available, the bias-corrected geostationary LST ($LSAFLST$) is updated. This is done taking into account the uncertainty of both sets of observations using a Kalman Filter:

$$LSAFLST_a = LSAFLST + K(LSAFLST - Sentinel3LST_{nor})$$

where $LSAFLST_a$ is the updated LST at the hour t and K is the Kalman gain with the range [0, 1], computed as:

$$K = PH^T(HPH^T + R) - 1$$

with P being the uncertainty of the geostationary observation $LSAFLST$ and R the uncertainty of the Sentinel 3 observation at time step t. Both uncertainties are available for each individual pixel and time-step. H, the observation operator, is 1 as there is no difference between model and observation space. Normally, the update in a Kalman Filter is propagated over time through a dynamic model. Here, there is no such prognostic model to predict LST, thus we correct all subsequent hourly $LSAFLST$ observations by the same amount until the next observation is available.

4 Analysis and validation

4.1 Incoming radiation fluxes

Comprehensive validation studies in literature against pyranometer measurements show the high accuracy of the LSAF radiation products; see e.g. Carrer et al. (2019b) or Lopes et al. (2022). A validation of the LSAF SW_{in} data by Roerink et al. (2012) against the CarboEurope flux tower network shows a very high accuracy, corroborated by comparing the satellite product with available radiation estimates from about 300 operational weather stations. Our own validation of both the LSAF SW_{in} and LW_{in} products shows a similar good performance, with Pearson's correlation coefficients consistently above 0.9. Figure 1 (top panels) show the correlation coefficients for all *in situ* sites in Europe for the 2018–2019 period. They are generally higher for SW_{in} than for LW_{in}. In terms of the root-mean-squared error (RMSE), SW_{in} and LW_{in} perform similarly across all sites. Few stations with a considerably worse match between observations and *in situ* data are located in Belgium for SW_{in}, and around the Alps for LW_{in}.
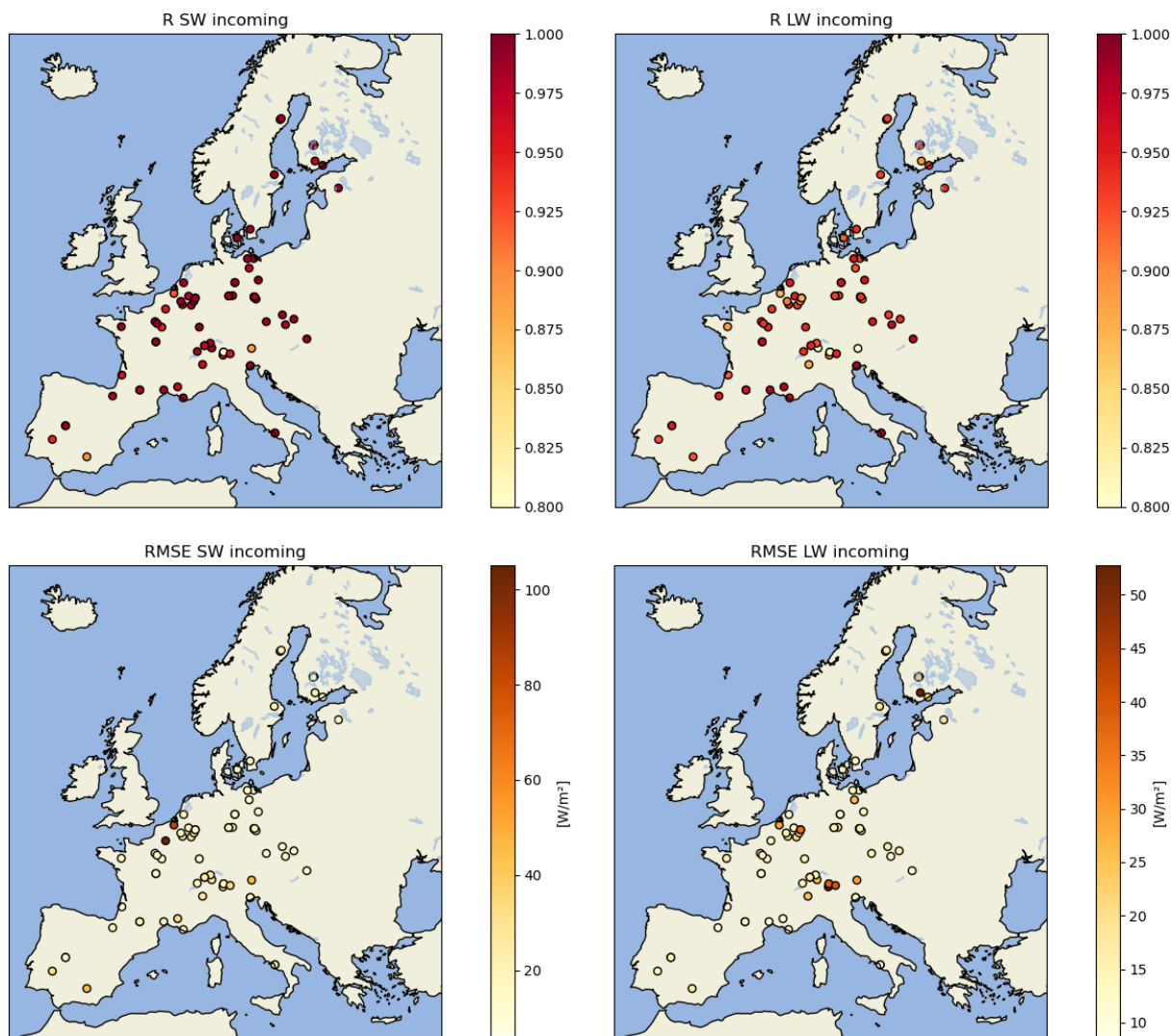
Figure 1. Validation of SW_{in} and LW_{in} from LSAF across Europe for 2018–2019 in terms of Pearson's correlation coefficient (R, top panels) and root mean squared error (RMSE, lower panels).

4.2 Land surface temperature

220 Extensive validation of the LSAF and Sentinel 3 LST products has already been performed (see below). Both have an average accuracy below 1.5 K, although it varies across space and time. Our goal is to combine their individual strengths in terms of spatial and temporal resolution to obtain an enhanced representation of landscape heterogeneity. For an in-depth quantitative validation of the Sentinel 3 LST product we refer to Pérez-Planells et al. (2021). The LSAF LST products were validated by Trigo et al. (2008a), Göttsche et al. (2013), Göttsche et al. (2016), Martins et al. (2019) and Trigo et al. (2021). Here the

225   validation against *in situ* data is carried out not directly on LST but on LW_{out} – see section 3.3

Figure 2 shows the mean annual LST for 2018–2019 for two regions in Europe according to either the LSAF LST or
the final merged LSAF/Sentinel 3 LST. The downscaled LST product shows significantly more spatial detail, especially in
heterogeneous or topographic complex areas such as the Central System in Madrid (top row) or the Rhine Valley and its
230   surrounding mountainous areas (bottom row). Instead of the 2018–2019 LST average, Figure 3 shows the original LSAF LST
and the downscaled LST product for 30th June 2018 as an example day.
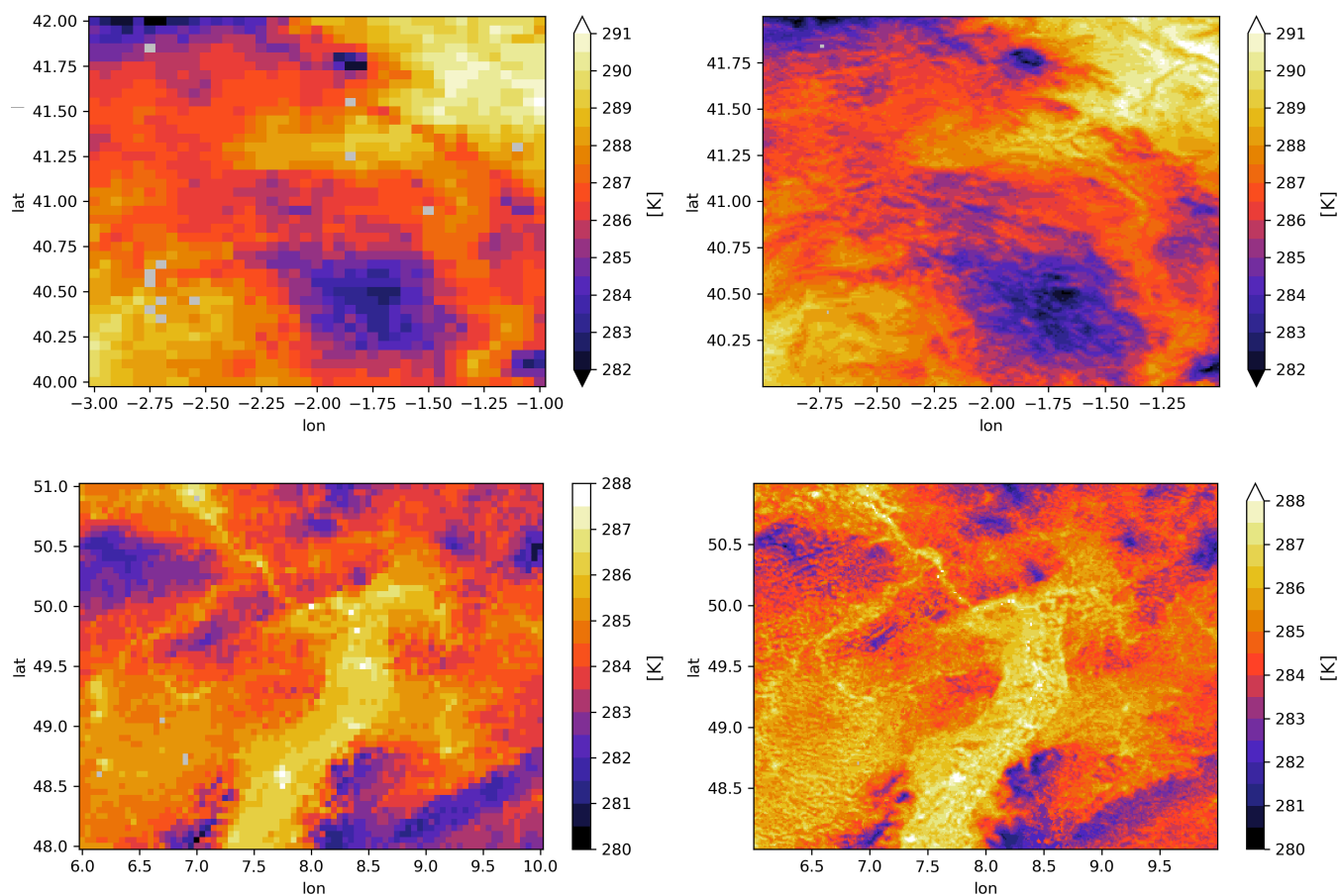
Figure 2. Mean LSAF LST (left) and merged LSAF/Sentinel 3 LST (right) for 2018–2019, showing a part of the Iberian Peninsula (top) and
the southern Rhine Valley (bottom).
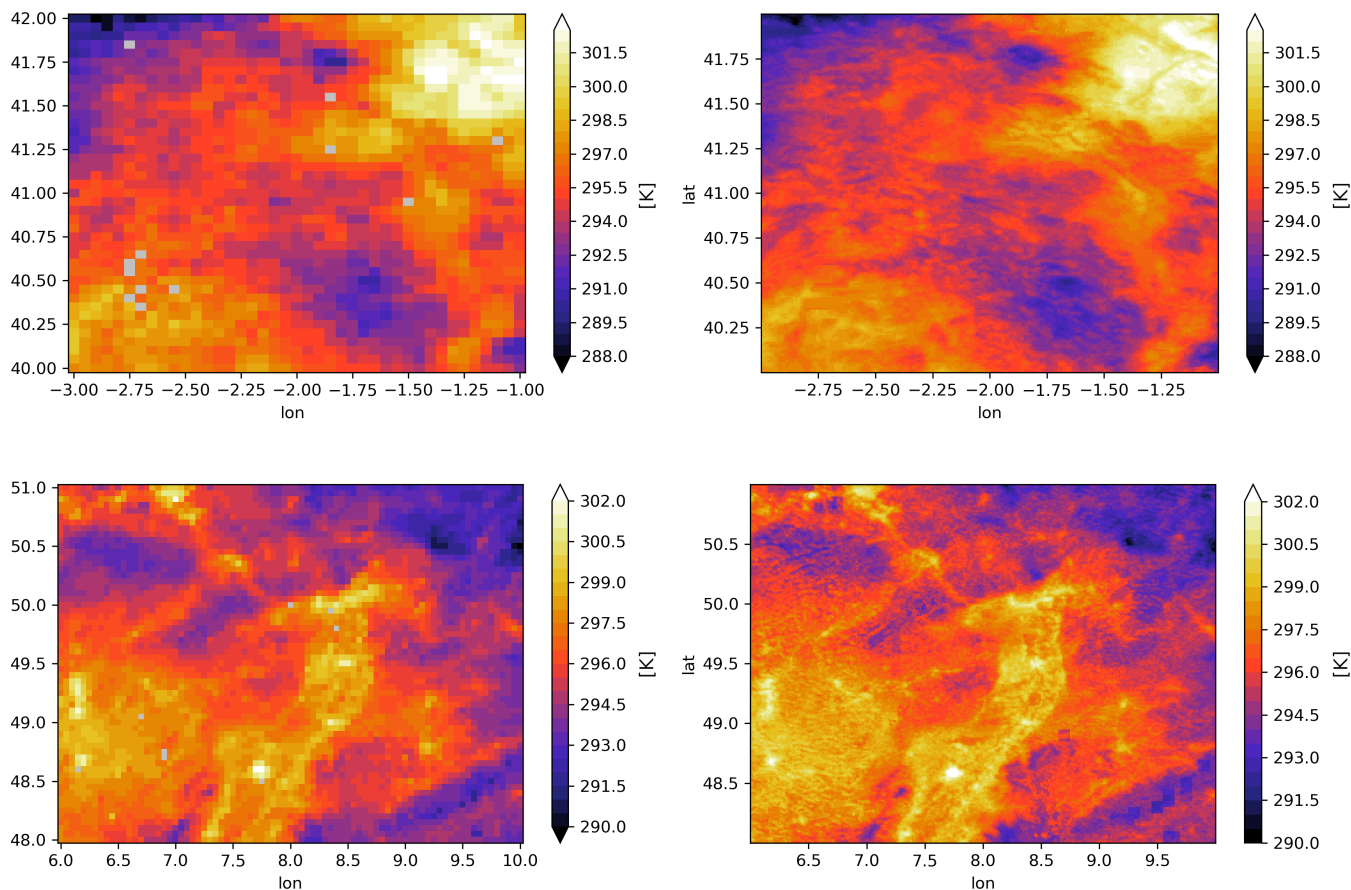
Figure 3. LSAF LST (left) and merged LSAF/Sentinel 3 LST (right) for 30th June 2018, showing the centre of the Iberian Peninsula (top) and the southern Rhine Valley (bottom).

4.3 Land surface albedo

Figure 4 shows the 2018–2019 mean albedo from LSAF and from the downscaled albedo product across parts of the Rhine valley, as well as the values for a single day, analogous to the LST figures 2–3. The effect of the downscaling in enhancing the spatial detail of the LSAF albedo retrievals based on PROBA-V retrievals is evident; see (e.g.) the distinct areas of low albedo surrounding the Rhine valley covered by forests and the higher albedo areas within the valley.
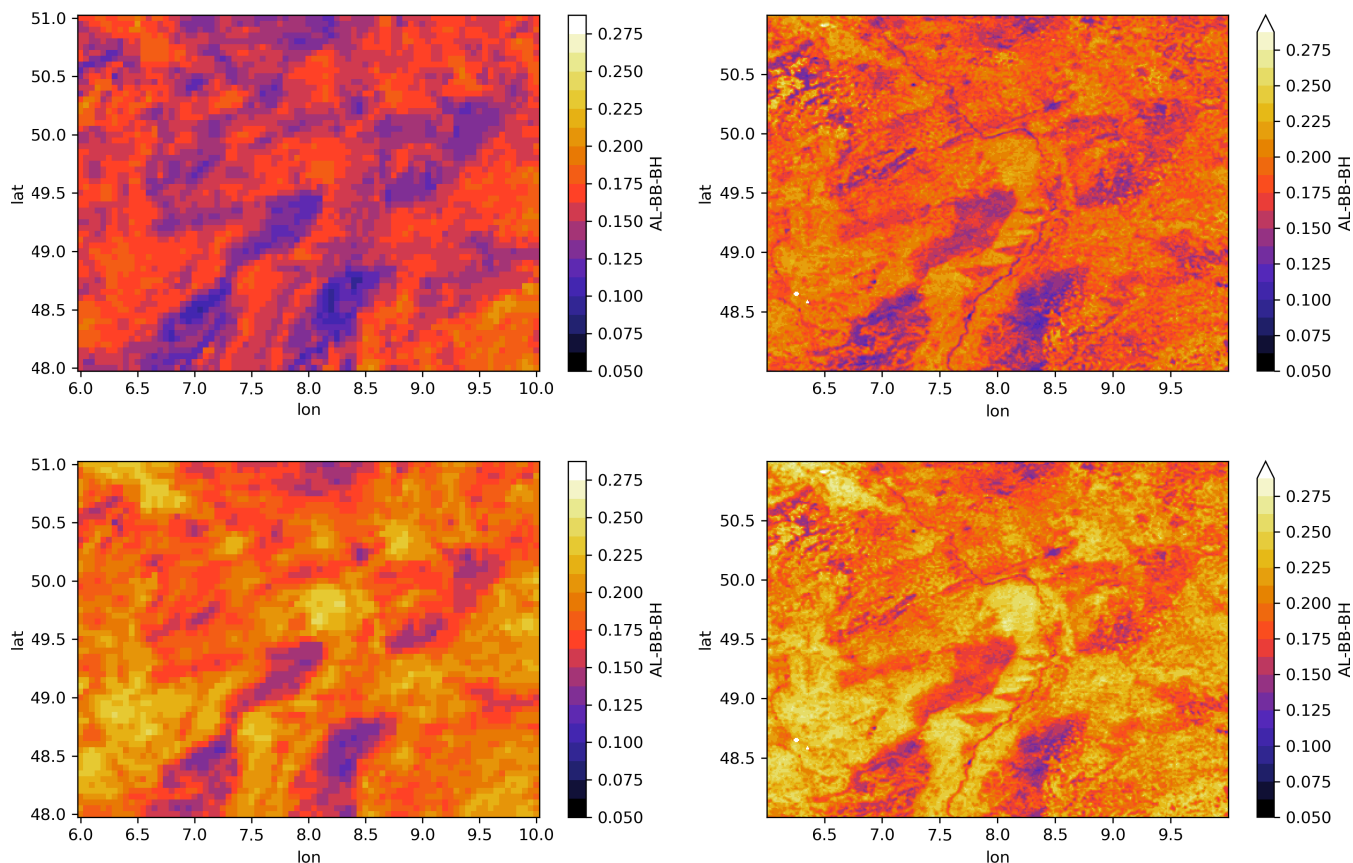
Figure 4. Mean albedo from LSAF (top left) and the downscaled dataset (top right) for 2018–2019, as well as the retrievals for the 30th June 2018 for LSAF (bottom left) and the downscaled albedo product (bottom right). Maps depict the southern Rhine valley.

4.4 Outgoing radiation fluxes

SW_{out} estimates, resulting from combining LSAF SW_{in} with either LSAF α or with the downscaled α dataset, are validated against *in situ* data. Likewise, LW_{out}, using either LSAF LST or the downscaled LST product, are also compared against *in situ* data. This validation therefore shows to what extent the downscaling of SW_{out} and LW_{out} influences the accuracy, and not only spatial detail, as shown in sections 4.2 and 4.3.

Figure 5 shows the distribution of the RMSE across the available sites for the 2018–2019 period. Both RMSE for SW_{out} and LW_{out} are lower when compared to using data from LSAF only, with a mean of 13.9 W/m^2 vs. 15.3 W/m^2 for SW_{out}, and 9.5 W/m^2 vs 10 W/m^2 for LW_{out}). For LW_{out}, 35 from 63 sites show an improvement, whereas for SW_{out} only 38 out of 78 sites show an improvement. Figure 6 shows the RMSE spatially for LSAF (left) and the difference to the downscaled products (right).
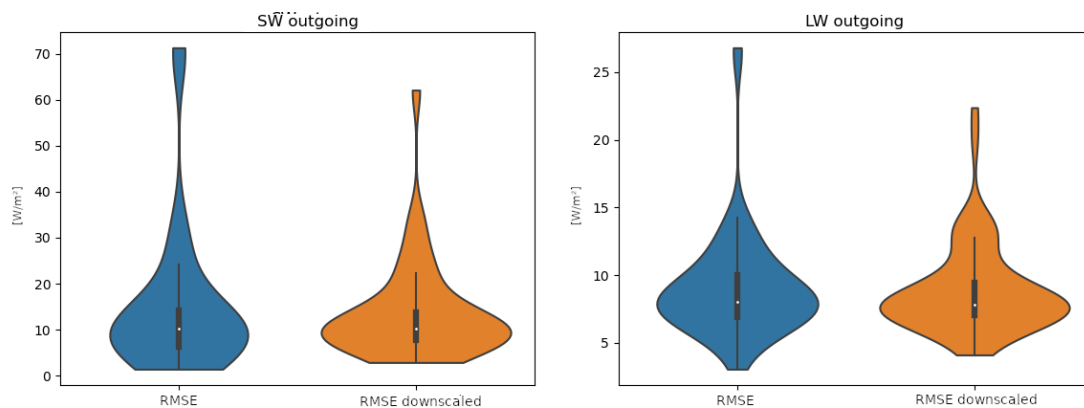
Figure 5. Validation in terms of RMSE of LSAF (blue) and downscaled (orange) LW_{out} (left) and SW_{out} (right). Based on the period 2018–2019 and a total of 63 and 78 *in situ* sites for LW_{out} and SW_{out}, respectively.
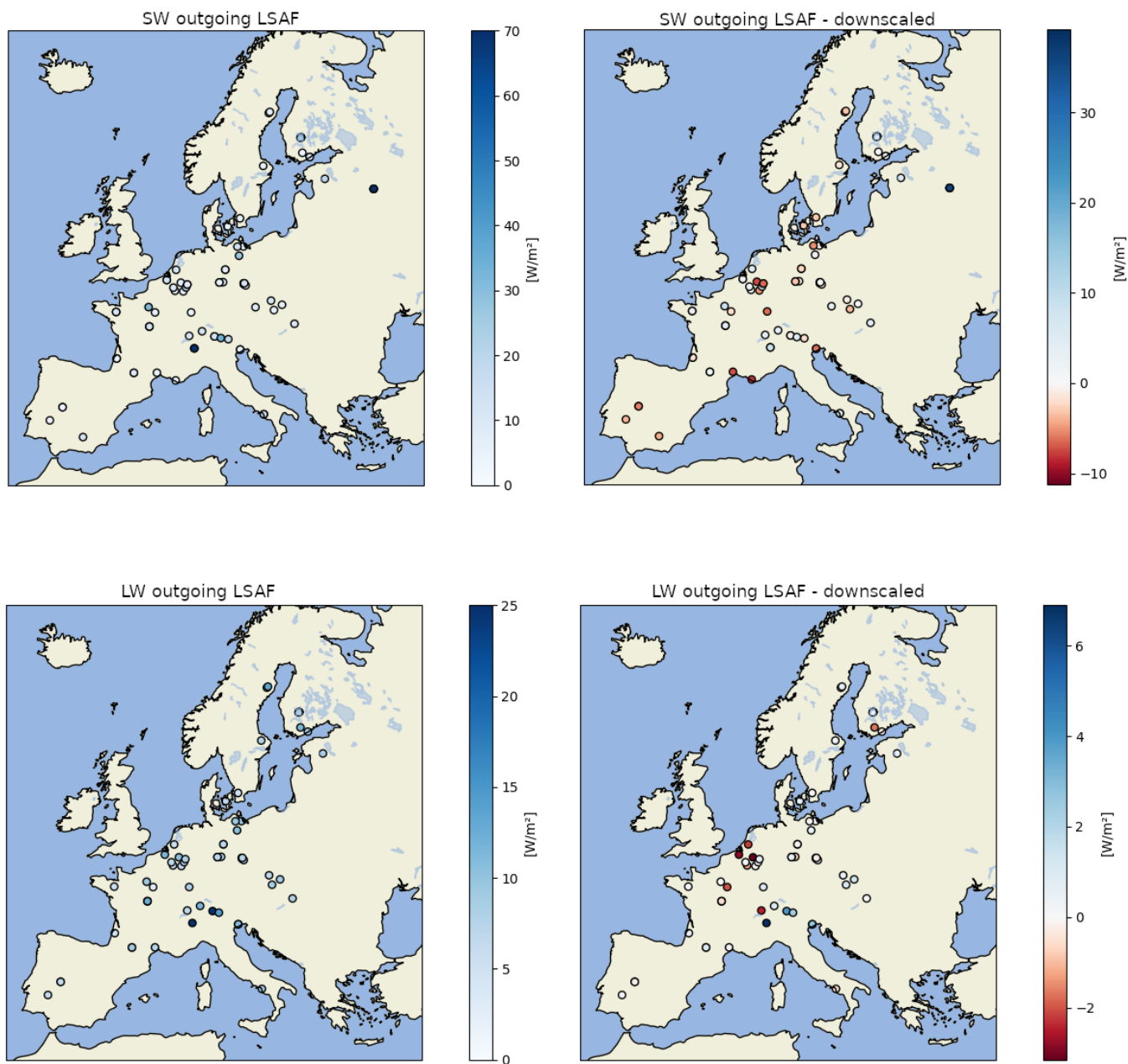
Figure 6. Validation of SW_{out} (top) and LW_{out} (bottom) in terms of RMSE. Based on LSAF only (left) and the difference to the downscaled products on the right; blue colours on the right panels indicate a better performance of the downscaled products.

4.5 Surface net radiation

The downscaled SNR dataset, resulting from the hourly SW_{in} and LW_{in} as well as the downscaled hourly SW_{out} and LW_{out}, is validated against the available *in situ* data at daily time scales. On average, the downscaled product has a RMSE of 21.6

250 W/m^2 vs 22.6 W/m^2 for the MSG only product. From the available 52 in situ sites, 38 show an improvement in terms of RMSE. Figure 7 show the distribution of RMSE values across sites, with the results shown spatially in Figure 8.
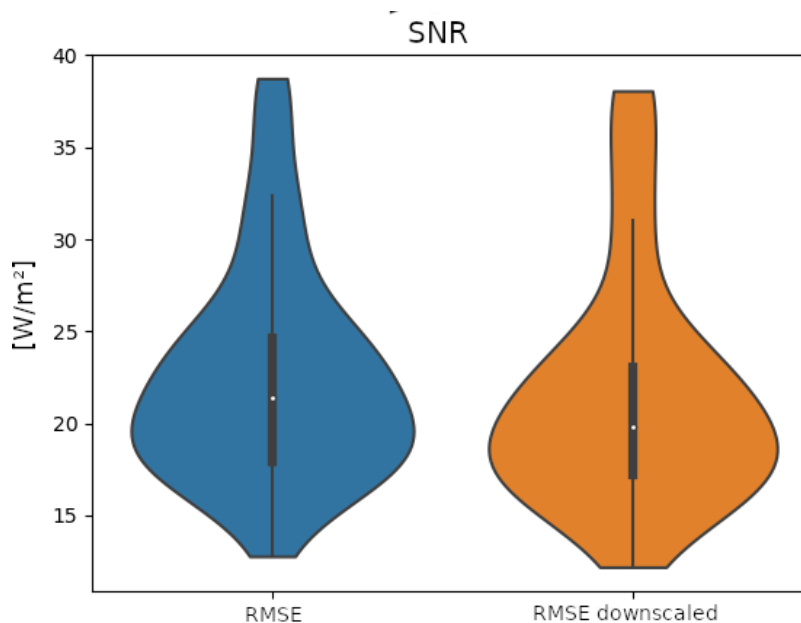
Figure 7. Validation of SNR in terms of RMSE, for LSAF (left) and the downscaled dataset (right). Based on 52 *in situ* sites distributed across Europe for 2018–2019.
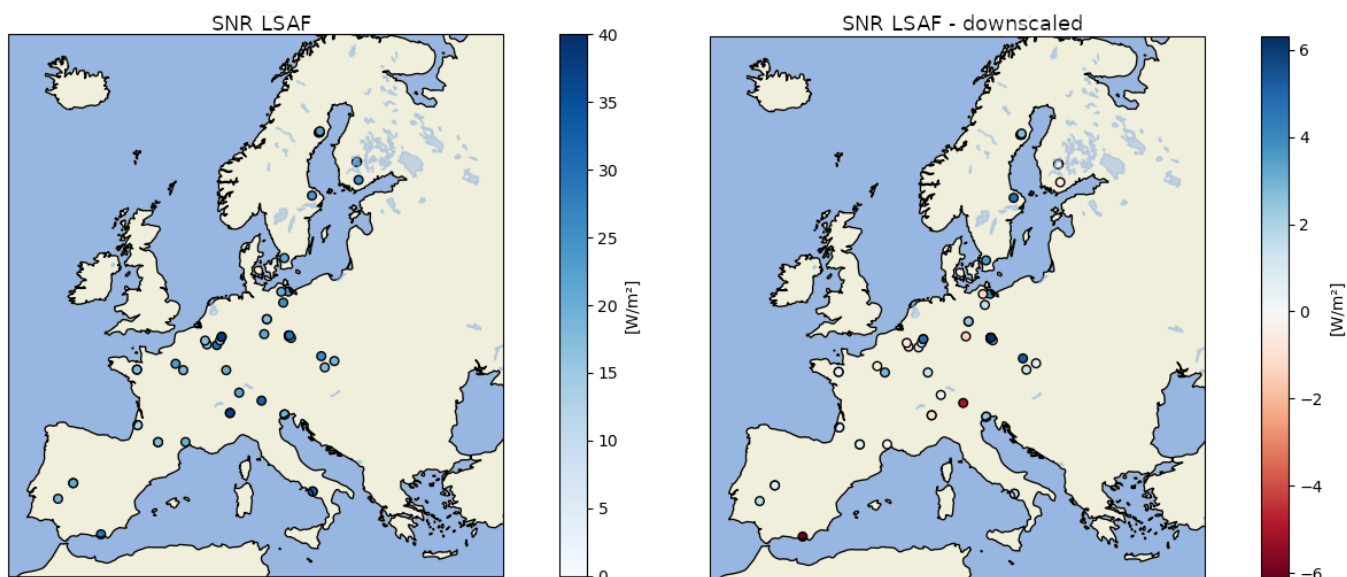
Figure 8. Validation of SNR in terms of RMSE using LSAF only (left) and the difference to the downscaled product on the right; blue colors on the right map indicate a better performance of the downscaled product.

5 Conclusions

Both surface net radiation and land surface temperature are key input variables for many land surface and hydrological models. With increased efforts to simulate land surface processes at higher spatial resolution, the lack of high-resolution gap-free SNR and LST datasets is an issue. Heterogeneity is then primarily driven by land surface properties for which high-resolution datasets are more frequently available (e.g. soil texture, vegetation phenology).

Here, we presented a methodology to combine the advantages of geostationary observations at high temporal resolution with observations from polar-orbiting satellites at high spatial resolution, resulting in a gap-free all-sky LST and net radiation dataset for 2018–2019 across Europe. Based on an operational data input stream, the method can be easily updated on a close to near-real time basis. While the input datasets already show a very high accuracy, moderate improvements in RMSE were achieved in addition to a substantial increase in spatial heterogeneity and representativeness.

Any future enhancements in the source products would directly lead to improvements in future releases of the downscaled datasets. While the developed methodology of merging two different sets of LST retrievals includes the bias correction of LSAF towards Sentinel 3 (see section 3.3), the use of Sentinel 3 SLSTR emissivity maps when computing the outgoing longwave radiation LW_{out} should also be considered in future product updates. In addition, the presented results are based on the use of LST retrievals from the Sentinel 3A satellite and data from Sentinel 3B will be incorporated in future updates. For consistency, the use of Sentinel-3 based albedo instead of PROBA-V will also be explored.

A limitation in the downscaling methodology is that, while bias correction and product-specific uncertainties are employed, there is no dynamic model to propagate the updates from the Sentinel 3 LST assimilation at the daytime or nighttime overpass time to the subsequent hours. To paliate this issue, we apply equivalent updates to the subsequent hourly LSAF observations, separately for temporal daytime/nighttime windows. Alternative approaches – such as the attenuation of the assimilation impact over time – could be explored in the future based on a more in-depth analysis of the diurnal cycle. Given that the hourly products are however mainly used to generate daily aggregates, the effect might be less important than at finer temporal resolutions. While the validation presented concentrated on daily aggregates, the availability of hourly LST and radiation products does make it possible to resolve the diurnal cycle, which can be a requirement for certain models. The final downscaled LST and net radiation product at daily time-scale is available under https://zenodo.org/record/7008066.YwKeDlrMIb1; updates and temporal extensions of the data records are planned in the near future.

6 Data availability

The daily SNR and LST datasets for 2018–2019 are available for scientific use under https://doi.org/10.5281/zenodo.7008066 / https://doi.org/10.5281/zenodo.7026612 as netcdf files (RNETdaily_lon_lat.nc and LSTdaily_lon_lat.nc), see Rains (2022a) and Rains (2022b).

Appendix A: Downscaling of LSAF LST with Sentinel 3 LST

The downscaling/merging of the LSAF with Sentinel 3 based LST retrievals described in section 3.3 is shown in more detail here. Figure A1 shows as an example the mean Sentinel 3 LST and the bias towards LSAF observations for daytime (10am. UTC) observations. Across the domain the bias is neither systematically negative nor positive, again highlighting the similarities between LSAF and Sentinel 3 observations, and it is more linked to geographic features and specific areas. The bias is corrected for per-pixel (after adjusting each Sentinel 3 observation to the Sentinel 3 mean overpass time rounded to the full hour using the diurnal information from the hourly LSAF data) allowing for the subsequent assimilation step.
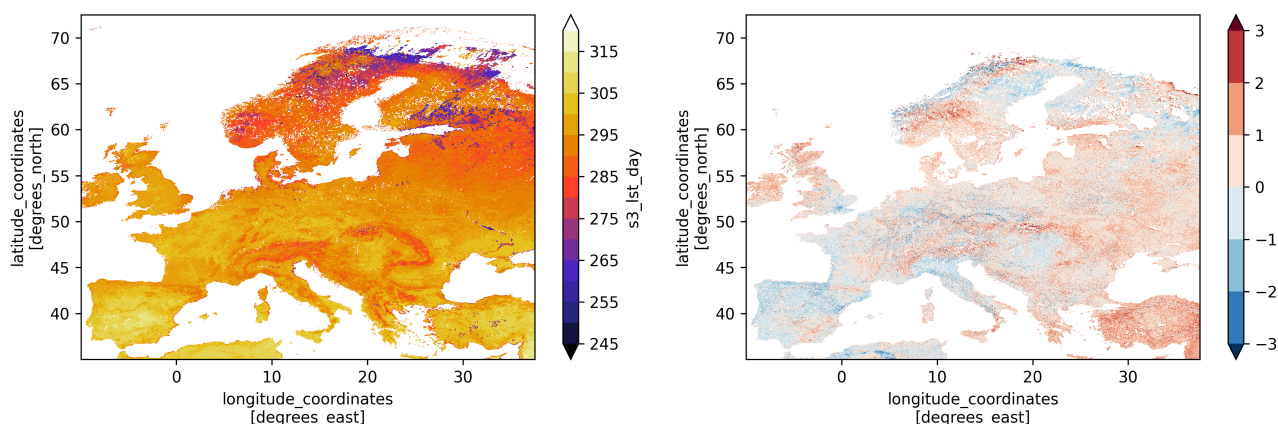
Figure A1. Mean LST of Sentinel 3 daytime (10am. UTC) observations (left) and bias towards LSAF observations (right).

During the assimilation step the Sentinel 3 observations will have an impact on the final downscaled LST dataset based on the respective uncertainties of both Sentinel 3 and LSAF LST retrievals. Figure A2 shows for a single day some assimilation diagnostics, such as the Sentinel 3 observations themselves, the uncertainty map of the Sentinel 3 observations (top middle) and the uncertainty of the LSAF observations (top right). The Kalman Gain (bottom left) is based on the two uncertainties and a value of 1 would fully trust the Sentinel 3 observation, whereas 0 would result in no assimilation update. The difference, i.e. innovation between the Sentinel 3 observation and LSAF LST, is shown in the lower middle. The increment, the actual update, is the innovation multiplied by the Kalman Gain and is shown in the bottom right.
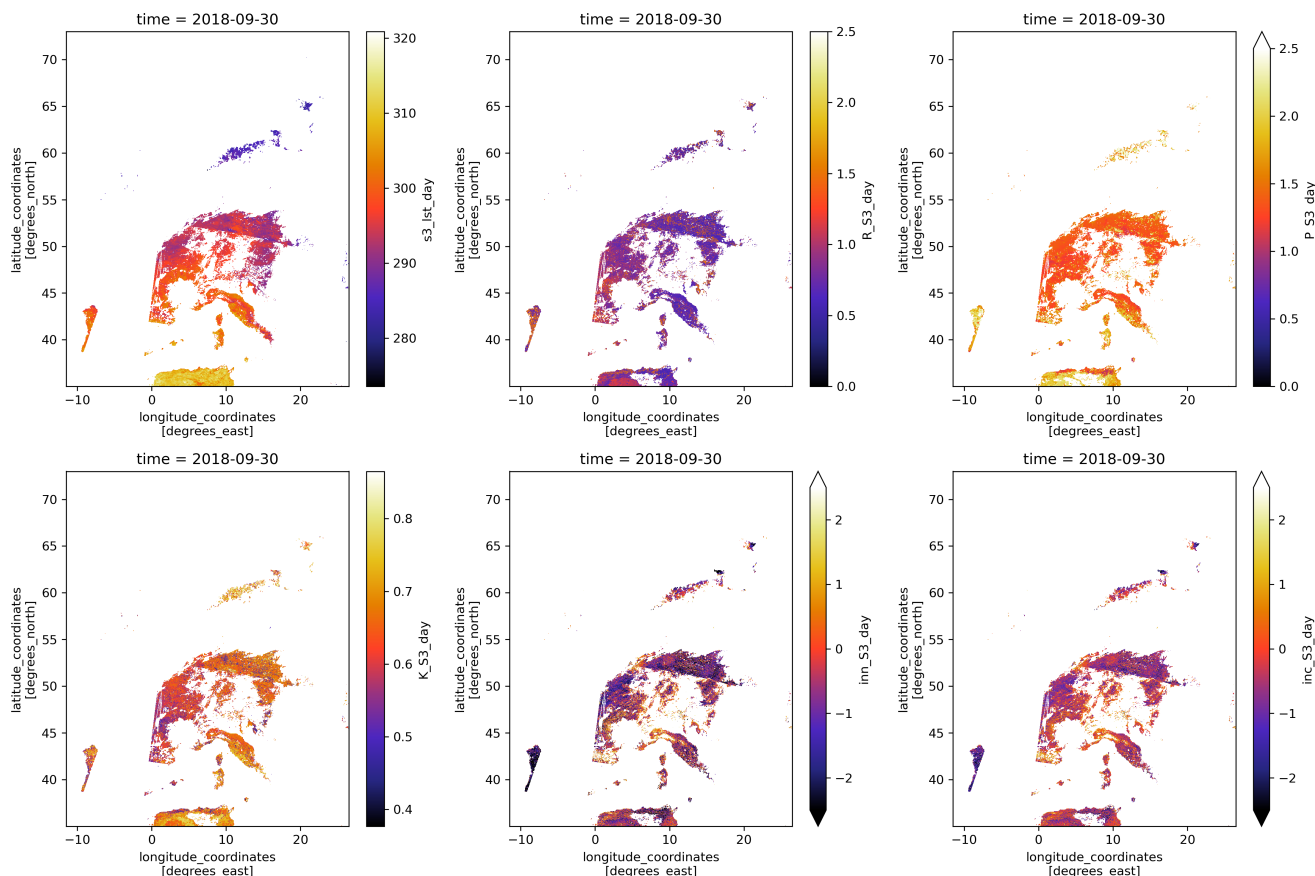
Figure A2. Sentinel 3 LST retrievals (top left), uncertainty of Sentinel 3 LST retrievals (top middle), uncertainty of LSAF LST retrievals (top right) and Kalman Gain (bottom left), innovations (bottom middle), increments (bottom right).

300   Figure A3 shows the 2018–2019 mean assimilation diagnostics for the daytime Sentinel 3 assimilation. The innovation, i.e. the difference between the Sentinel 3 LST observations and the LSAF LST, is fairly close to zero showing that the bias correction results in observations being spread evenly around the background estimate, i.e. LSAF, as intended. The mean increment, the actual correction applied to the LSAF estimates, shows the same spatial patterns. The mean Kalman Gain shows to what extent either the LSAF or Sentinel 3 observations are trusted based on the uncertainty estimates of both sets of observations.

305
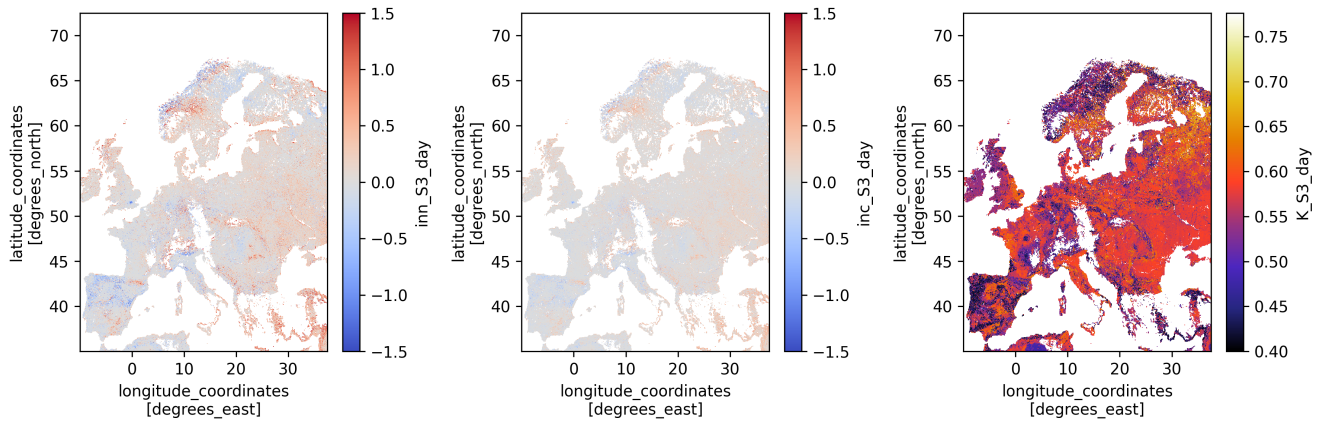
Figure A3. Mean Innovation (left), increments (middle) and Kalman Gain (right) for daytime Sentinel 3 LST assimilation.

Competing interests. No competing interests are present.

References

Carrer, D., Lafont, S., Roujean, J.-L., Calvet, J.-C., Meurey, C., Le Moigne, P., and Trigo, I.: Incoming solar and infrared radiation derived from METEOSAT: Impact on the modeled land water and energy budget over France, Journal of Hydrometeorology, 13, 504–520, 2012.

310 Carrer, D., Moparthy, S., Lellouch, G., Ceamanos, X., Pinault, F., Freitas, S. C., and Trigo, I. F.: Land surface albedo derived on a ten daily basis from Meteosat Second Generation Observations: The NRT and climate data record collections from the EUMETSAT LSA SAF, Remote Sensing, 10, 1262, 2018.

Carrer, D., Ceamanos, X., Moparthy, S., Vincent, C., C. Freitas, S., and Trigo, I. F.: Satellite Retrieval of Downwelling Shortwave Surface Flux and Diffuse Fraction under All Sky Conditions in the Framework of the LSA SAF Program (Part 1: Methodology), Remote Sensing,

315 11, https://doi.org/10.3390/rs11212532, 2019a.

Carrer, D., Moparthy, S., Vincent, C., Ceamanos, X., C. Freitas, S., and Trigo, I. F.: Satellite Retrieval of Downwelling Shortwave Surface Flux and Diffuse Fraction under All Sky Conditions in the Framework of the LSA SAF Program (Part 2: Evaluation), Remote Sensing, 11, https://doi.org/10.3390/rs11222630, 2019b.

Chapin, F. S., Matson, P. A., Mooney, H. A., and Vitousek, P. M.: Principles of terrestrial ecosystem ecology, 2002.

320 Delwiche, K. B., Knox, S. H., Malhotra, A., Fluet-Chouinard, E., McNicol, G., Feron, S., Ouyang, Z., Papale, D., Trotta, C., Canfora, E., et al.: FLUXNET-CH 4: a global, multi-ecosystem dataset and analysis of methane seasonality from freshwater wetlands, Earth system science data, 13, 3607–3689, 2021.

Dewitte, S. and Clerbaux, N.: Measurement of the Earth Radiation Budget at the Top of the Atmosphere—A Review, Remote Sensing, 9, https://doi.org/10.3390/rs9111143, 2017.

325 Donlon, C., Berruti, B., Mecklenberg, S., Nieke, J., Rebhan, H., Klein, U., Buongiorno, A., Mavrocordatos, C., Frerick, J., Seitz, B., Goryl, P., Féménias, P., Stroede, J., and Sciarra, R.: The Sentinel-3 Mission: Overview and status, in: 2012 IEEE International Geoscience and Remote Sensing Symposium, pp. 1711–1714, https://doi.org/10.1109/IGARSS.2012.6351194, 2012.

Driemel, A., Augustine, J., Behrens, K., Colle, S., Cox, C., Cuevas-Agulló, E., Denn, F. M., Duprat, T., Fukuda, M., Grobe, H., et al.: Baseline Surface Radiation Network (BSRN): structure and data description (1992–2017), Earth System Science Data, 10, 1491–1501, 2018.

330 Faroux, S., Kaptué Tchuenté, A., Roujean, J.-L., Masson, V., Martin, E., and Moigne, P. L.: ECOCLIMAP-II/Europe: A twofold database of ecosystems and surface parameters at 1 km resolution based on satellite information for use in land surface, meteorological and climate models, Geoscientific Model Development, 6, 563–582, 2013.

Geiger, B., Carrer, D., Franchisteguy, L., Roujean, J.-L., and Meurey, C.: Land surface albedo derived on a daily basis from Meteosat Second Generation observations, IEEE Transactions on Geoscience and Remote Sensing, 46, 3841–3856, 2008.

335 Ghent, D., Corlett, G., Göttsche, F.-M., and Remedios, J.: Global land surface temperature from the along-track scanning radiometers, Journal of Geophysical Research: Atmospheres, 122, 12–167, 2017.

Ghilain, N.: Chapter 16 - Continental Scale Monitoring of Subdaily and Daily Evapotranspiration Enhanced by the Assimilation of Surface Soil Moisture Derived from Thermal Infrared Geostationary Data, in: Satellite Soil Moisture Retrieval, edited by Srivastava, P. K., Petropoulos, G. P., and Kerr, Y. H., pp. 309–332, Elsevier, https://doi.org/https://doi.org/10.1016/B978-0-12-803388-3.00016-4, 2016.

340 Ghilain, N., Arboleda, A., Barrios, J., and Gellens-Meulenberghs, F.: Water interception by canopies for remote sensing based evapotranspiration models, International Journal of Remote Sensing, 41, 2934–2945, 2020.

Göttsche, F.-M., Olesen, F., and Bork-Unkelbach, A.: Validation of land surface temperature derived from MSG/SEVIRI with in situ measurements at Gobabeb, Namibia, International Journal of Remote Sensing, https://doi.org/10.1080/01431161.2012.716539, 2013.

Göttsche, F.-M., Olesen, F., Trigo, I., Bork-Unkelbach, A., and Martin, M.: Long Term Validation of Land Surface Temperature Retrieved
345   from MSG/SEVIRI with Continuous in-Situ Measurements in Africa, Remote Sensing, 8, 410, https://doi.org/10.3390/rs8050410, 2016.

Heiskanen, J., Brümmer, C., Buchmann, N., Calfapietra, C., Chen, H., Gielen, B., Gkritzalis, T., Hammer, S., Hartman, S., Herbst, M., et al.:
     The Integrated Carbon Observation System in Europe, Bulletin of the American Meteorological Society, pp. 1–54, 2021.

Jia, A., Liang, S., Jiang, B., Zhang, X., and Wang, G.: Comprehensive Assessment of Global Surface Net Radiation Products and Uncertainty
     Analysis, Journal of Geophysical Research: Atmospheres, 123, 1970–1989, https://doi.org/https://doi.org/10.1002/2017JD027903, 2018.

350 Kato, S., Rose, F. G., Rutan, D. A., Thorsen, T. J., Loeb, N. G., Doelling, D. R., Huang, X., Smith, W. L., Su, W., and Ham, S.-H.: Surface
     Irradiances of Edition 4.0 Clouds and the Earth's Radiant Energy System (CERES) Energy Balanced and Filled (EBAF) Data Product,
     Journal of Climate, 31, 4501 – 4527, https://doi.org/10.1175/JCLI-D-17-0523.1, 2018.

Köppen, W. and Geiger, R.: Handbuch der klimatologie, vol. 1, Gebrüder Borntraeger Berlin, 1936.

Lopes, F. M., Dutra, E., and Trigo, I. F.: Integrating Reanalysis and Satellite Cloud Information to Estimate Surface Downward Long-Wave
355   Radiation, Remote Sensing, 14, https://doi.org/10.3390/rs14071704, 2022.

Maes, W. and Steppe, K.: Estimating evapotranspiration and drought stress with ground-based thermal remote sensing in agriculture: a
     review, Journal of Experimental Botany, 63, 4671–4712, 2012.

Martins, J., Trigo, I. F., Ghilain, N., Jimenez, C., Göttsche, F.-M., Ermida, S. L., Olesen, F.-S., Gellens-Meulenberghs, F., and Arboleda, A.:
     An all-weather land surface temperature product based on MSG/SEVIRI observations, Remote Sensing, 11, 3044, 2019.

360 Nie, J., Ren, H., Zheng, Y., Ghent, D., and Tansey, K.: Land Surface Temperature and Emissivity Retrieval From Night-
     time Middle-Infrared and Thermal-Infrared Sentinel-3 Images, IEEE Geoscience and Remote Sensing Letters, 18, 915–919,
     https://doi.org/10.1109/LGRS.2020.2986326, 2021.

Peres, L. F. and DaCamara, C. C.: Emissivity maps to retrieve land-surface temperature from MSG/SEVIRI, IEEE Transactions on Geo-
     science and Remote Sensing, 43, 1834–1844, 2005.

365 Poyatos, R., Granda, V., Flo, V., Adams, M. A., Adorján, B., Aguadé, D., Aidar, M. P. M., Allen, S., Alvarado-Barrientos, M. S., Anderson-
     Teixeira, K. J., Aparecido, L. M., Arain, M. A., Aranda, I., Asbjornsen, H., Baxter, R., Beamesderfer, E., Berry, Z. C., Berveiller, D.,
     Blakely, B., Boggs, J., Bohrer, G., Bolstad, P. V., Bonal, D., Bracho, R., Brito, P., Brodeur, J., Casanoves, F., Chave, J., Chen, H., Cisneros,
     C., Clark, K., Cremonese, E., Dang, H., David, J. S., David, T. S., Delpierre, N., Desai, A. R., Do, F. C., Dohnal, M., Domec, J.-C.,
     Dzikiti, S., Edgar, C., Eichstaedt, R., El-Madany, T. S., Elbers, J., Eller, C. B., Euskirchen, E. S., Ewers, B., Fonti, P., Forner, A., Forrester,
370   D. I., Freitas, H. C., Galvagno, M., Garcia-Tejera, O., Ghimire, C. P., Gimeno, T. E., Grace, J., Granier, A., Griebel, A., Guangyu, Y.,
     Gush, M. B., Hanson, P. J., Hasselquist, N. J., Heinrich, I., Hernandez-Santana, V., Herrmann, V., Hölttä, T., Holwerda, F., Irvine, J.,
     Isarangkool Na Ayutthaya, S., Jarvis, P. G., Jochheim, H., Joly, C. A., Kaplick, J., Kim, H. S., Klemedtsson, L., Kropp, H., Lagergren,
     F., Lane, P., Lang, P., Lapenas, A., Lechuga, V., Lee, M., Leuschner, C., Limousin, J.-M., Linares, J. C., Linderson, M.-L., Lindroth, A.,
     Llorens, P., López-Bernal, A., Loranty, M. M., Lüttschwager, D., Macinnis-Ng, C., Maréchaux, I., Martin, T. A., Matheny, A., McDowell,
375   N., McMahon, S., Meir, P., Mészáros, I., Migliavacca, M., Mitchell, P., Mölder, M., Montagnani, L., Moore, G. W., Nakada, R., Niu, F.,
     Nolan, R. H., Norby, R., Novick, K., Oberhuber, W., Obojes, N., Oishi, A. C., Oliveira, R. S., Oren, R., Ourcival, J.-M., Paljakka, T., Perez-
     Priego, O., Peri, P. L., Peters, R. L., Pfautsch, S., Pockman, W. T., Preisler, Y., Rascher, K., Robinson, G., Rocha, H., Rocheteau, A., Röll,
     A., Rosado, B. H. P., Rowland, L., Rubtsov, A. V., Sabaté, S., Salmon, Y., Salomón, R. L., Sánchez-Costa, E., Schäfer, K. V. R., Schuldt,
     B., Shashkin, A., Stahl, C., Stojanović, M., Suárez, J. C., Sun, G., Szatniewska, J., Tatarinov, F., Tesař, M., Thomas, F. M., Tor-ngern, P.,
380   Urban, J., Valladares, F., van der Tol, C., van Meerveld, I., Varlagin, A., Voigt, H., Warren, J., Werner, C., Werner, W., Wieser, G., Wingate,
     L., Wullschleger, S., Yi, K., Zweifel, R., Steppe, K., Mencuccini, M., and Martínez-Vilalta, J.: Global transpiration data from sap flow

measurements: the SAPFLUXNET database, Earth System Science Data, 13, 2607–2649, https://doi.org/10.5194/essd-13-2607-2021, 2021.

Pérez-Planells, L., Niclòs, R., Puchades, J., Coll, C., Göttsche, F.-M., Valiente, J. A., Valor, E., and Galve, J. M.: Validation of Sentinel-3 SLSTR Land Surface Temperature Retrieved by the Operational Product and Comparison with Explicitly Emissivity-Dependent Algorithms, Remote Sensing, 13, https://doi.org/10.3390/rs13112228, 2021.

Rains, D.: LSTRAD, https://doi.org/10.5281/zenodo.7008066, 2022a.

Rains, D.: LSTRAD, https://doi.org/10.5281/zenodo.7026612, 2022b.

Roerink, G., Bojanowski, J., de Wit, A., Eerens, H., Supit, I., Leo, O., and Boogaard, H.: Evaluation of MSG-derived global radiation estimates for application in a regional crop model, Agricultural and Forest Meteorology, 160, 36–47, https://doi.org/https://doi.org/10.1016/j.agrformet.2012.02.006, 2012.

Stephens, G. L., Li, J., Wild, M., Clayson, C. A., Loeb, N., Kato, S., L'ecuyer, T., Stackhouse, P. W., Lebsock, M., and Andrews, T.: An update on Earth's energy balance in light of the latest global observations, Nature Geoscience, 5, 691–696, 2012.

Trigo, I. F., Monteiro, I. T., Olesen, F., and Kabsch, E.: An assessment of remotely sensed land surface temperature, Journal of Geophysical Research: Atmospheres, 113, 2008a.

Trigo, I. F., Peres, L. F., DaCamara, C. C., and Freitas, S. C.: Thermal land surface emissivity retrieved from SEVIRI/Meteosat, IEEE Transactions on Geoscience and Remote Sensing, 46, 307–315, 2008b.

Trigo, I. F., Barroso, C., Viterbo, P., Freitas, S. C., and Monteiro, I. T.: Estimation of downward long-wave radiation at the surface combining remotely sensed data and NWP data, Journal of Geophysical Research: Atmospheres, 115, 2010.

Trigo, I. F., Dacamara, C. C., Viterbo, P., Roujean, J.-L., Olesen, F., Barroso, C., Camacho-de Coca, F., Carrer, D., Freitas, S. C., García-Haro, J., et al.: The satellite application facility for land surface analysis, International Journal of Remote Sensing, 32, 2725–2744, 2011.

Trigo, I. F., Ermida, S. L., Martins, J. P., Gouveia, C. M., Göttsche, F.-M., and Freitas, S. C.: Validation and consistency assessment of land surface temperature from geostationary and polar orbit platforms: SEVIRI/MSG and AVHRR/Metop, ISPRS Journal of Photogrammetry and Remote Sensing, 175, 282–297, https://doi.org/https://doi.org/10.1016/j.isprsjprs.2021.03.013, 2021.

Verma, M., Fisher, J. B., Mallick, K., Ryu, Y., Kobayashi, H., Guillaume, A., Moore, G., Ramakrishnan, L., Hendrix, V., Wolf, S., Sikka, M., Kiely, G., Wohlfahrt, G., Gielen, B., Roupsard, O., Toscano, P., Arain, A., and Cescatti, A.: Global Surface Net-Radiation at 5 km from MODIS Terra, Remote Sensing, 8, https://doi.org/10.3390/rs8090739, 2016.

Wielicki, B. A., Barkstrom, B. R., Harrison, E. F., Lee III, R. B., Smith, G. L., and Cooper, J. E.: Clouds and the Earth's Radiant Energy System (CERES): An earth observing system experiment, Bulletin of the American Meteorological Society, 77, 853–868, 1996.

Young, A. H., Knapp, K. R., Inamdar, A., Hankins, W., and Rossow, W. B.: The international satellite cloud climatology project H-Series climate data record product, Earth System Science Data, 10, 583–593, 2018.

Zheng, Y., Ren, H., Guo, J., Ghent, D., Tansey, K., Hu, X., Nie, J., and Chen, S.: Land surface temperature retrieval from sentinel-3A sea and land surface temperature radiometer, using a split-window algorithm, Remote Sensing, 11, 650, 2019.